

# Magnetic tunnel junction nanopillars surrounded by resistive Si switches: a logic-in-memory device

Yu Zhang<sup>1,2,3</sup>, Xiaoyang Lin<sup>1,2</sup>, Jean-Paul Adam<sup>3</sup>, Guillaume Agnus<sup>3</sup>, Wenlong Cai<sup>1,2</sup>, Jean-Rene Coudeville<sup>3</sup>, Nathalie Isac<sup>3</sup>, Jianlei Yang<sup>1,2</sup>, Huaiwen Yang<sup>1,2</sup>, Wang Kang<sup>1,2</sup>, Kaihua Cao<sup>1,2,4</sup>, Hushan Cui<sup>1,4,5</sup>, Deming Zhang<sup>1,2</sup>, Youguang Zhang<sup>1,2</sup>, Chao Zhao<sup>1,4,5</sup>, Weisheng Zhao<sup>1,2\*</sup>, and Dafine Ravelosona<sup>3</sup>

<sup>1</sup>Fert Beijing Institute, BDBC, Beihang University, Beijing 100191, China

<sup>2</sup>School of Electronic and Information Engineering, Beihang University, Beijing 100191, China

<sup>3</sup>Centre de Nanosciences et de Nanotechnologies (C2N), University of Paris-Sud, Université Paris-Saclay, Orsay 91405, France

<sup>4</sup>Institute of Microelectronics, Chinese Academy of Sciences, Beijing, 100029, China

<sup>5</sup>University of Chinese Academy of Sciences (UCAS), Beijing 100049, P. R. China

**Emerging, fast-speed, high-capacity and low-power non-volatile memories (NVMs) are becoming crucial enablers of current information communication technologies. However, they all suffer from intrinsic limitations, which restrict the range of their applications. Here, we report a nanoscale logic-in-memory device that combines the advantages of Magnetic RAM (MRAM) and Resistive RAM (RRAM) into a single structure. The device is based on a resistively enhanced MRAM (Re-MRAM) element integrated with a magnetic tunnel junction (MTJ) nanopillar encapsulated by a SiO<sub>x</sub>-based polymer with surrounding resistive nanoscale Si filaments. The Re-MRAM features magnetic switching together with a high ON/OFF ratio that can reach 1000% and multilevel resistance behaviour. As a result, the Re-MRAM combines logic computation and memory in a single device and significantly reduces the data traffic, paving the way towards CMOS-compatible non-von Neumann architectures in which logic and memory are unified and providing the perspective to build up fast, dense and highly power-efficient computing systems.**

Mainstream computing systems suffer from power limitations due to the static power induced by leakage currents and the dynamic power required for data traffic between memory and logic circuits<sup>1</sup>. Non-volatile memories (NVMs) combined with novel computing architecture are considered as the most promising solution to overcome this power wall and continue progressing computing performance<sup>2-5</sup>. For instance, logic-in-memory architectures based on closely integrating NVMs with logic circuits have been proposed to minimize the power required and pave the way towards normally-off/instant-on computing<sup>6-9</sup>. Along this line, two of the most promising NVMs, *i.e.*, Magnetic RAM (MRAM)<sup>10-15</sup> and Resistive RAM (RRAM)<sup>16-20</sup>, have attracted increasing interest. MRAM combines excellent scalability, endurance, low-power, fast read/write properties, and it is compatible with the back-end process of complementary metal-oxide-semiconductor (CMOS) technology. RRAM combines a high storage density with 3D packing, a high ON/OFF ratio, low-energy consumption, good scalability and compatibility with CMOS technology. Unfortunately, both of these technologies suffer from major intrinsic limitations. Regarding MRAM, the low ON/OFF ratio of tunnel magnetoresistance (TMR) and the

limited thermal stability below 20 nm have become a major issue<sup>12</sup>. In particular, the last generation, *i.e.*, perpendicular Spin Transfer Torque (STT)-MRAM, in which magnetic fast switching is induced by a current, has a maximum TMR of 220%<sup>21-23</sup>, which leads to a small margin during read operations and, consequently, to low fault tolerance<sup>24,25</sup>. In contrast, RRAM has a relatively low access speed and finite endurance<sup>18,19</sup>. A single integrated structure merging the merits of MRAM as a computing element and RRAM as a memory element would become an ideal device for a logic-in-memory architecture. In particular, a much better power efficiency<sup>2</sup> would be possible since the data traffic between the memory and logic elements would be suppressed. In this regard, a recent proposal is based on the use of a MgO-based magnetic tunnel junction (MTJ) that can exhibit both magnetic switching (MS) and resistive switching (RS)<sup>26-29</sup>. In this case, the RS process has been related to oxygen vacancy defects in the engineered MgO barrier, making the MTJ a RRAM element. However, this approach suffers from the fact that a trade-off exists between MS and RS as both depend on the properties of MgO, and after operating as an RS memory, the MTJ becomes inoperative as an MS memory. In this paper, we demonstrate the proof of concept of a resistively enhanced MRAM (Re-MRAM) logic-in-memory device based on a regular MTJ nanopillar surrounded by resistive Si filaments that behave as resistive switches.

Fig. 1a shows a schematic view of the Re-MRAM device made of an in-plane magnetized CoFe(B)-MgO MTJ nanopillar and a SiO<sub>x</sub>-based polymer encapsulation layer. In the MTJ structure, the MgO tunnel barrier is sandwiched by two CoFe(B)-based magnetic thin films corresponding to the free and reference layers. Driven by either an in-plane magnetic field or a spin-polarized current, the MTJ can be switched between parallel (P) and anti-parallel (AP) states, leading to two resistance states, namely,  $R_P$  and  $R_{AP}$ , respectively. Fig. 1b shows a cross-sectional transmission electron microscope (TEM) image of the device. The magnetic films were patterned into submicron-sized ellipses with dimension ranging from  $80 \times 160 \text{ nm}^2$  to  $100 \times 240 \text{ nm}^2$  using electron beam lithography (EBL) and an angle-optimized ion beam etching (IBE) process. Then, the MTJ nanopillars were encapsulated by a Si-O-based insulator fabricated by baking a polymer (Accuflo)<sup>30</sup> at a reduced temperature. As shown in Fig. 1c, the cross-sectional TEM image of the MTJ stacks indicate the presence of the crystallized MgO tunnel barrier and CoFe(B) layers with body-centred cubic (bcc) structures after annealing the magnetic stack.

Fig. 2 indicates the very peculiar resistive behaviour of the device under an applied voltage resulting from the combination of current-induced magnetization switching (CIMS) and voltage-induced resistive switching (VIRS). Indeed, as shown in the typical I-V curves of Fig. 2a, bipolar (in which positive and negative voltages have the opposite effect) VIRS was observed in the absence of external magnetic fields, with a maximum voltage of 0.8 V. For this measurement, the MTJ was set to either the P or AP state using the external magnetic field before the measurement. Clear resistive switching behaviour was observed for which the SET and RESET voltages could be identified. Fig. 2b shows the corresponding R-V curve for the P and AP configurations, in which the low-resistance state (LRS) and high-resistance state (HRS) can be observed. Here, the LRS is approximately  $600 \Omega$ , irrespective of the magnetic configurations, and the HRS is approximately  $1100 \Omega$  and  $1300 \Omega$  for P and AP states, respectively. In this example, the typical ON/OFF ratio for the AP state was approximately 120% but ratios reaching 1000% were observed (see Supplementary Fig. S2). Notably, magnetization switching between the P and AP states was not observed during the voltage sweep. Additionally, we observed that the SET and

RESET voltages were independent of the magnetic configuration. Fig. 2c shows the R-V curve under the in-plane magnetic fields<sup>31</sup> that were used to assist CIMS. Pure CIMS was not obtained here at low voltages due to the thickness of the free layer. The maximum voltage applied was below 0.2 V in order to avoid VIRS and maintain the RHS. We observed CIMS assisted by the magnetic fields of  $H_{ext}^{AP \rightarrow P} = +110 \text{ Oe}$  and  $H_{ext}^{P \rightarrow AP} = -104 \text{ Oe}$ , with typical current densities of  $J_c^{AP \rightarrow P} = 1.7 \times 10^5 \text{ A/cm}^2$  and  $J_c^{P \rightarrow AP} = -0.8 \times 10^5 \text{ A/cm}^2$ , respectively. These results show that CIMS and VIRS could be controlled independently. To observe both effects, a voltage was applied between  $\pm 0.8 \text{ V}$  under magnetic fields (Fig. 2d). In this case, we clearly observed that the VIRS and CIMS effects could act simultaneously.

The results shown in Fig. 2 are different from those of previous findings involving RS due to the filamentary current path in the MgO barrier. First, in our experiment, we observed bipolar switching instead of unipolar switching (SET and RESET were caused by applying voltages of the same polarity). In addition, we observed both MS and RS in the same R-V loop; this result suggests two independent origins for the CIMS and RS processes. To gain more insight, we carefully investigated the microstructures of the elements. The nanofabrication process of the device consisted of encapsulating the CoFe(B)-MgO nanopillars with a SiO<sub>x</sub> insulator in contact with the edges of the nanostructure (See Fig. 1b, 3a). In the following, we provide evidence that the VIRS behaviour was induced by the presence of the resistive Si filaments at the edges of the nanopillars. Microscopic structure characterizations were performed using energy-dispersive X-ray spectroscopy (EDS). Fig. 3b and 3c indicates the presence of the Ta and Si elements detected by measuring the characteristic peaks of the Ta- $\text{La}$  (8.145 KeV) and Si- $\text{K}$  series lines, respectively. Note that since the Ta- $\text{M}\alpha$  (1.709 KeV) and Si- $\text{K}\alpha$  (1.739 KeV) were separated by only 30 eV, and the detector could not resolve these lines<sup>32,33</sup>. The detection results of both the Si and Ta elements overlapped, as seen in Fig. 3c. Thus, the comparison between Fig. 3b and 3c clearly evidences that Si aggregation occurred along the sidewall of the nanopillars with a typical width of 5-10 nm. In addition, high-resolution TEM (HRTEM) images of the nanodevice indicate the presence of nanocrystals with a typical size of 5-10 nm embedded in the amorphous SiO<sub>x</sub> along the edges of the nanopillars (See Fig. 3d). The microstructural analysis (Fig. 3) and the electrical results of Fig. 2 are consistent with recent studies, which have evidenced that RS in a SiO<sub>x</sub> matrix can be induced by the presence of embedded Si nanocrystals<sup>16,34-36</sup>. More precisely, when an SET voltage is applied, the Si nanocrystals can grow locally by favouring an electrochemical reduction process of SiO<sub>x</sub>  $\rightarrow$  Si, which induces a Si pathway (Si filaments) along the current flow direction, whereas a RESET voltage can favour the Si  $\rightarrow$  SiO<sub>x</sub> inverse process. This mechanism corresponds to a point-switching filament process involving local break and bridge evolution.

One important question is related to the presence of Si nanocrystals in our devices. It has been shown that the forming process of Si nanocrystals can be induced in pure SiO<sub>x</sub> matrix at low temperatures by etching the SiO<sub>x</sub><sup>16,37</sup>. In this case, the Si filaments can germinate at the edges of the SiO<sub>x</sub> elements due to the presence of defects. In our case, the SiO<sub>x</sub> matrix surrounding the nanopillars was obtained by spinning a polymer (Accuflo) and transforming it into an insulator using an annealing process at approximately 300 °C. During the annealing process, the edges of the nanopillars involving damages induced by the etching process (see Methods) could serve as seed interfaces to nucleate the Si nanocrystals. In addition, the crystalline character of the MTJ may have also favoured the germination of the Si nanocrystals. Furthermore, another interesting

feature related to the microstructural properties of the devices is that the ON/OFF ratio for the RS was strongly related to the TMR value for the MS (see Fig. 4a). In particular, the ON/OFF ratio increased when the TMR value was reduced. This result suggests that when the TMR ratio was low, a point-switching filament process could occur, whereas when the TMR was higher, the conduction through the Si filaments was not active. Notably, the TMR value in the CoFeB-MgO-based MTJs was related to the Fe-O bonds at the CoFe(B)/MgO interface<sup>38-42</sup>. In particular, an over-oxidized interface led to a lower TMR value. In this regard, the results shown in Fig. 4a indicate that the oxidation of the edges of the nanopillars could play a joint role in both the TMR value and the nucleation of the nanocrystals. Indeed, an EDS line-scan measured from the SiO<sub>x</sub> matrix into the MgO barrier (see Fig. 4b, 4c) indicates that both Si and O aggregated at the edges of the nanopillars on a scale of 10 nm with a ratio of silicon and oxygen elements that was much higher at the edges than in the SiO<sub>x</sub> matrix. The fact that bipolar behaviour was observed here for the SET and RESET processes may have been related to the presence of mobile oxygen ions. Within this edge transition, we also noticed an interdiffusion layer including Mg, Fe and Co elements.

Based on the microstructure described above, a proposed schematic of the Re-MRAM device is presented in Fig. 5a and 5b consisting of an MTJ-based element connected in parallel with a Si filament element. Four distinct configurations with different resistance states are presented in Fig. 5b, corresponding to states (1) ~ (4), as indicated in Fig. 2d. When the Si filaments are not conductive (RESET process), the current mainly goes through the MTJ, resulting in an HRS, and when the Si filaments become conductive, the current mainly flows through the Si filaments, resulting in a LRS. To verify the proposed device model, simulations were performed using a compact model integrating a physical-based STT-MTJ<sup>43</sup> and a bipolar metal-insulator-metal (MIM) resistive junction<sup>44,45</sup> connected in parallel. Fig. 5c shows that the R-V curve of Fig. 2d combining CIMS and VIRS was reproduced quite well by taking  $R_{AP} = 1390 \Omega$ ,  $R_P = 1160 \Omega$ ,  $R_{HRS} = 64500 \Omega$ , and  $R_{LRS} = 660 \Omega$ .

The multilevel states of the Re-MRAM device were investigated and are presented in Fig. 6. Fig. 6a shows seven consecutive R-V curves indicating that different resistive states could be reached using a single device. Each R-V curve corresponds to a different degree of the Si oxidation pathway, which was randomly induced by the combination of a local strong electric field and heating during the point-switching filament process. Fig. 6b presents a Re-MRAM device that exhibited eight different states by combining two magnetic states (P and AP) with four different resistive states of the Si filaments. A larger TMR ratio was achieved for higher resistance states; this result reflects that the lower resistance of the MTJ dominated the current pathway. Furthermore, the data retention of the Re-MRAM device was tested for four different resistance states (see Fig. 6c). All the configurations exhibited robust non-volatile properties. Finally, we demonstrated that the functionalities of the Re-MRAM device evidenced here can be used to combine storage and computation in a single element. Based on the same model used in Fig. 5, Supplementary Fig. S3 presents a working logic-in-memory device in which fast computation was realized in the MTJ, and the results were stored in the RRAM filaments.

In conclusion, we have demonstrated the first nanoscale logic-in-memory device that is compatible with the back-end process of CMOS technology by combining a Magnetic RAM (MRAM) connected in parallel with a Resistive RAM (RRAM) without increasing the dimension of the memory cell. This approach enables new perspectives for ultralow-power logic-in-memory

architectures in which storage and computation can be unified in a single element. The proof of concept demonstrated here involves low TMR values, but in principle, our approach allows one to independently optimize the properties of the MRAM and RRAM elements. It should also be noted that for logic-in-memory applications, a high ON/OFF ratio is not a prerequisite for storing the computing results in the RRAM element. Finally, the new features of the Re-MRAM device are also very promising for bio-inspired computing<sup>46,47</sup> and checkpoint applications<sup>48</sup>.

## Methods

The magnetic multilayers were deposited onto  $\text{SiO}_2$ -coated Si wafers using a combination of RF and DC sputtering in a Canon-Anelva system. From the substrate side, the MTJ structure consisted of the following layers: Ta(5)/Ru(15)/Ta(5)/Ru(15)/Ta(5)/Ru(5)/PtMn(20)/CoFeB(1.5)/CoFe(2.0)/Ru(0.85)/CoFeB(1.5)/CoFe(1.5)/MgO(0.8)/CoFe(1.5)/CoFeB(1.5)/Ru(2)/Ta(5)/Ru(10) (the numbers are the nominal thicknesses in nanometers). The bottom and top layers, Ta(5 nm)/Ru(15 nm)/Ta(5 nm)/Ru(15 nm)/Ta(5 nm)/Ru(5 nm) and Ru(2 nm)/Ta(5 nm)/Ru(10 nm), respectively, were designed for the CIPT measurements using a CAPRES microprobe tool. The typical TMR ratio and the resistive-area product of the unpatterned films were  $\sim 144\%$  and  $\sim 19 \Omega \cdot \mu\text{m}^2$ , respectively. After deposition, annealing was performed at 350 °C for 1 h with an in-plane applied magnetic field of 1 T under a vacuum of  $10^{-6}$  Torr. The magnetization curves were measured using a MicroSense vibrating sample magnetometer system at room temperature (see Supplementary Fig. S1).

The devices were patterned using a self-aligned lift-off and back-end-of-line (BEOL) process. Submicron-sized ellipses with sizes ranging from  $80 \times 160 \text{ nm}^2$  to  $100 \times 240 \text{ nm}^2$  were obtained using EBL with a ZEP520A positive resist deposited on top of a 150 nm Ta layer, followed by platinum (Pt) deposition and a lift-off process. The Pt patterns were used as a protective mask to etch down the 150 nm tantalum (Ta) layer using inductively coupled plasma (ICP). Then, the Ta patterns were used as a hard mask to etch down the MTJs using an optimized IBE process to avoid sidewall redisposition. A VM652 promoter and Accuflo T-25 Spin-on Polymer (produced by Honeywell) were sequentially spin coated, followed by a low-temperature curing process (below 300°C) for encapsulating the patterned structure in the  $\text{SiO}_x$ . The encapsulation layer was patterned into  $40 \times 60 \mu\text{m}^2$  elements using ICP. Finally, Cr/Au top electrodes were fabricated utilizing a lift-off approach.

The cross-sectional samples were prepared by using a focused ion beam in the plane of the long axis of the ellipse. The HRTEM, scanning TEM (STEM) and EDS mapping/line scanning were performed using a JEM-ARM200F transmission electron microscope operating at 200 keV.

The fabricated devices were characterized using DC-transport measurements under in-plane magnetic fields (with a precision below  $1 \times 10^{-3} \text{ Oe}$ ) with a two-probe geometry at room temperature. A bias voltage (or current) was applied to the top electrode, while the bottom electrode was grounded. The voltage-pulse (or current-pulse) durations were  $\tau_p = 200 \text{ ms}$ , and the remanent resistance of the Re-MRAM device was measured under a low bias between each voltage (or current) change.

The compact model of the device was written using Verilog-A language and evaluated in a Cadence Spectra environment. The compact model integrated a physical-based STT-MTJ and a bipolar MIM resistive junction connected in parallel. Magnetic fields were not considered in the simulation.

## References

<sup>1</sup> Roy, K., Mukhopadhyay, S. & Mahmoodi-Meimand, H. Leakage current mechanisms and leakage reduction techniques in deep-submicrometer CMOS circuits. *Proc. IEEE.* **91**, 305-327 (2003).

<sup>2</sup> Wong, H.S.P. & Salahuddin, S. Memory leads the way to better computing. *Nature Nanotech.* **10**, 191-194 (2015).

<sup>3</sup> Ando, K. et al. Spin-transfer torque magnetoresistive random-access memory technologies for normally off computing (invited). *J. Appl. Phys.* **115**, 172607 (2014).

<sup>4</sup> Turkyilmaz, O. et al. RRAM-based FPGA for "Normally Off, Instantly On" applications. *Proc. Int. Symp. Nanosc. Archit.* **101-108**, (2012).

<sup>5</sup> Kawahara, T. Scalable Spin-Transfer Torque RAM Technology for Normally-Off Computing. *IEEE Des. Test Comput.* **28**, 52-62 (2011).

<sup>6</sup> Matsunaga, S. et al. MTJ-based nonvolatile logic-in-memory circuit, future prospects and issues. *Proc. of the Conf. on Des. Automation and Test in Europe. European Design and Automation Assoc.* 433-435 (2009).

<sup>7</sup> Borghetti, J et al. 'Memristive' switches enable 'stateful' logic operations via material implication. *Nature.* **464**, 873-876 (2010).

<sup>8</sup> Mahmoudi, Hiwa, et al. Implication logic gates using spin-transfer-torque-operated magnetic tunnel junctions for intrinsic logic-in-memory. *Solid-State Electron.* **84**, 191-197 (2013).

<sup>9</sup> Linn E, Rosezin R, Tappertzhofen S, et al. Beyond von Neumann—logic operations in passive crossbar arrays alongside memory operations. *Nature Nanotech.* **23**, 305205 (2012).

<sup>10</sup> Kent, A.D. & Worledge, D.C. A new spin on magnetic memories. *Nature Nanotech.* **10**, 187-191 (2015).

<sup>11</sup> Apalkov, D. et al. Spin-Transfer Torque Magnetic Random Access Memory (STT-MRAM). *ACM J. Emerging Technol. Comput. Syst.* **9**, 13:1-13:35 (2013).

<sup>12</sup> Ikeda, S. et al. A perpendicular-anisotropy CoFeB-MgO magnetic tunnel junction. *Nature Mater.* **9**, 721-724 (2010).

<sup>13</sup> Katine, J. A., and Eric E. Fullerton. Device implications of spin-transfer torques. *J. Magn. Magn. Mater.* **320-7**, (2008).

<sup>14</sup> Yuasa, S. & Djayaprawira, D.D. Giant tunnel magnetoresistance in magnetic tunnel junctions with a crystalline MgO(001) barrier. *J. Phys. D: Appl. Phys.* **40**, R337-R354 (2007).

<sup>15</sup> Diao, Z. et al. Spin-transfer torque switching in magnetic tunnel junctions and spin-transfer torque random access memory. *J. Phys.: Condens. Matter* **19**, 165209 (2007).

<sup>16</sup> Yao, J., Sun, Z., Zhong, L., Natelson, D. & Tour, J.M. Resistive Switches and Memories from Silicon Oxide. *Nano Lett.* **10**, 4105-4110 (2010).

<sup>17</sup> Yang, J.J., Strukov, D.B. & Stewart, D.R. Memristive devices for computing. *Nature Nanotech.* **8**, 13-24 (2013).

<sup>18</sup> Wong, H.S.P. et al. Metal-Oxide RRAM. *Proc. IEEE.* **100**, 1951-1970 (2012).

<sup>19</sup> Akinaga, H. & Shima, H. Resistive Random Access Memory (ReRAM) Based on Metal Oxides. *Proc. IEEE*. **98**, 2237-2251 (2010).

<sup>20</sup> Chen, Y., Li, H H, Bayram, I. et al. Recent Technology Advances of Emerging Memories. *IEEE Des. Test.* **34**, 8-22 (2017).

<sup>21</sup> Song, Y.J. et al. Highly Functional and Reliable 8Mb STT-MRAM Embedded in 28nm Logic. In *Electron Devices Meeting (IEDM), 2016 IEEE International*.**27-2**, (2016).

<sup>22</sup> Tezuka, N. et al. Perpendicular Magnetic Tunnel Junctions With Low Resistance-Area Product: High Output Voltage and Bias Dependence of Magnetoresistance. *IEEE Magn. Lett.* **7**(2016).

<sup>23</sup> Ikeda, S. et al. Tunnel magnetoresistance of 604% at 300 K by suppression of Ta diffusion in CoFeB/MgO/CoFeB pseudo-spin-valves annealed at high temperature. *Appl. Phys. Lett.* **93**, 082508 (2008).

<sup>24</sup> Zhao, W., Chappert, C., Javerliac, V. & Noziere, J. High Speed, High Stability and Low Power Sensing Amplifier for MTJ/CMOS Hybrid Logic Circuits. *IEEE Trans. Magn.* **45**, 3784-3787 (2009).

<sup>25</sup> Kang, W. et al. Variation-Tolerant and Disturbance-Free Sensing Circuit for Deep Nanometer STT-MRAM. *IEEE Trans. Nanotechnol.* **13**, 1088-1092 (2014).

<sup>26</sup> Ventura, J. et al. Three-state memory combining resistive and magnetic switching using tunnel junctions. *J. Phys. D: Appl. Phys.* **40**, 5819-5823 (2007).

<sup>27</sup> Halley, D. et al. Electrical switching in Fe/Cr/MgO/Fe magnetic tunnel junctions. *Appl. Phys. Lett.* **92**, 212115 (2008).

<sup>28</sup> Krzyszczko, P., Reiss, G. & Thomas, A. Memristive switching of MgO based magnetic tunnel junctions. *Appl. Phys. Lett.* **95**, 112508 (2009).

<sup>29</sup> Teixeira, J.M. et al. Electroforming, magnetic and resistive switching in MgO-based tunnel junctions. *J. Phys. D: Appl. Phys.* **42**, 105407 (2009).

<sup>30</sup> Huang W, Kennedy J, Katsanes R. Planarization films for advanced microelectronic applications and devices and methods of production thereof. US patent 7,910,223 (2011).

<sup>31</sup> Lou, Xiaohua, et al. Demonstration of multilevel cell spin transfer switching in MgO magnetic tunnel junctions. *Appl. Phys. Lett.* **93**, 242502 (2008).

<sup>32</sup> Wagner C.D., Gale L.H., Raymond R.H. Two-dimensional chemical state plots: a standardized data set for use in identifying chemical states by x-ray photoelectron spectroscopy. *Anal. Chem.* **51**, 466-482 (1979).

<sup>33</sup> Hollerith, C., et al. Energy dispersive X-ray spectroscopy with microcalorimeters. *Nucl. Instr. and Meth. A*. **520**, 606-609 (2004).

<sup>34</sup> Yao, J., Zhong, L., Natelson, D. & Tour, J.M. Intrinsic resistive switching and memory effects in silicon oxide. *Appl. Phys. A* **102**, 835-839 (2011).

<sup>35</sup> Xia, G. et al. Direct observation of resistive switching memories behavior from nc-Si embedded in SiO<sub>2</sub> at room temperature. *J. Non-Cryst. Solids* **358**, 2348-2352 (2012).

<sup>36</sup> Wang, Y. et al. Resistive switching mechanism in silicon highly rich SiO<sub>x</sub> ( $x < 0.75$ ) films based on silicon dangling bonds percolation model. *Appl. Phys. Lett.* **102**, 042103 (2013).

<sup>37</sup> Zhou, Fei, et al. Discussion on device structures and hermetic encapsulation for SiO<sub>x</sub> random access memory operation in air. *Appl. Phys. Lett.* **105**, 163506 (2014).

<sup>38</sup> Zhang, X.G., Butler, W.H. & Bandyopadhyay, A. Effects of the iron-oxide layer in Fe-FeO-MgO-Fe tunneling junctions. *Phys. Rev. B* **68**, 092402 (2003).

<sup>39</sup> Timoshevskii, Vladimir, et al. Quantum transport modeling of the symmetric Fe/FeO0.5/MgO magnetic tunnel junction: the effects of correlations in the buffer layer. *J. Phys.: Condens. Matter* **26**(2014).

<sup>40</sup> Tusche, C., et al. Oxygen-induced symmetrization and structural coherency in Fe/MgO/Fe (001) magnetic tunnel junctions. *Phys. Rev. Lett.* **95**, 176101 (2005).

<sup>41</sup> Bonell, F., et al. Consequences of interfacial Fe-O bonding and disorder in epitaxial Fe/MgO/Fe(001) magnetic tunnel junctions. *Phys. Rev. B* **79**, 224405 (2009).

<sup>42</sup> Wang, Z. et al. Atomic-Scale Structure and Local Chemistry of CoFeB-MgO Magnetic Tunnel Junctions. *Nano Lett.* **16**, 1530-1536 (2016).

<sup>43</sup> Zhang, Y. et al. Compact Modeling of Perpendicular-Anisotropy CoFeB/MgO Magnetic Tunnel Junctions. *IEEE Trans. Electron Devices* **59**, 819-826 (2012).

<sup>44</sup> Rozenberg, M.J., Inoue, I.H. & Sanchez, M.J. Nonvolatile memory with multilevel switching: A basic model. *Phys. Rev. Lett.* **92**, 178302 (2004).

<sup>45</sup> Russo, Ugo, et al. Self-Accelerated Thermal Dissolution Model for Reset Programming in Unipolar Resistive-Switching Memory (RRAM) Devices. *IEEE Trans. Electron Devices* **56**, 193-200 (2009).

<sup>46</sup> Locatelli, N., Cros, V., & Grollier, J. *Nature Mater.* **13**, 11-20 (2013).

<sup>47</sup> Prezioso, M. et al. Training and operation of an integrated neuromorphic network based on metal-oxide memristors. *NATURE* **521**, 61-64 (2015).

<sup>48</sup> Xie, Y. Modeling, Architecture, and Applications for Emerging Memory Technologies. *IEEE Des. Test Comput.* **28**, 44-50 (2011).

## **Acknowledgements**

We would like to thank Li Huang and Xiufeng Han at the Beijing National Laboratory for Condensed Matter Physics (Chinese Academy of Sciences) and Sylvain Eimer and Fabien Bayle at the Centre de Nanosciences et de Nanotechnologies (University of Paris-Sud) for their technical support as well as Qunwen Leng (Goertek Corporation) for fruitful discussions.

## **Author contributions**

W.Z. and D.R conceived and supervised the project. Y.Z fabricated the devices and initiated the measurements. Y.Z, D.R and W.Z. wrote the manuscript. Y.Z, W.C. and J-P.A performed the measurements. G.A, N.I and J-R.C helped optimize the fabrication flow. K.C., H.C., and C.Z performed the TEM measurements. J.Y. and D.Z. carried out the compact model simulation. X.L., H.Y., W.K, and YG.Z, helped analyse the data. All authors discussed the results and implications.

## **Competing financial interests**

The authors declare no competing financial interests.

## Figures and Figure Legends

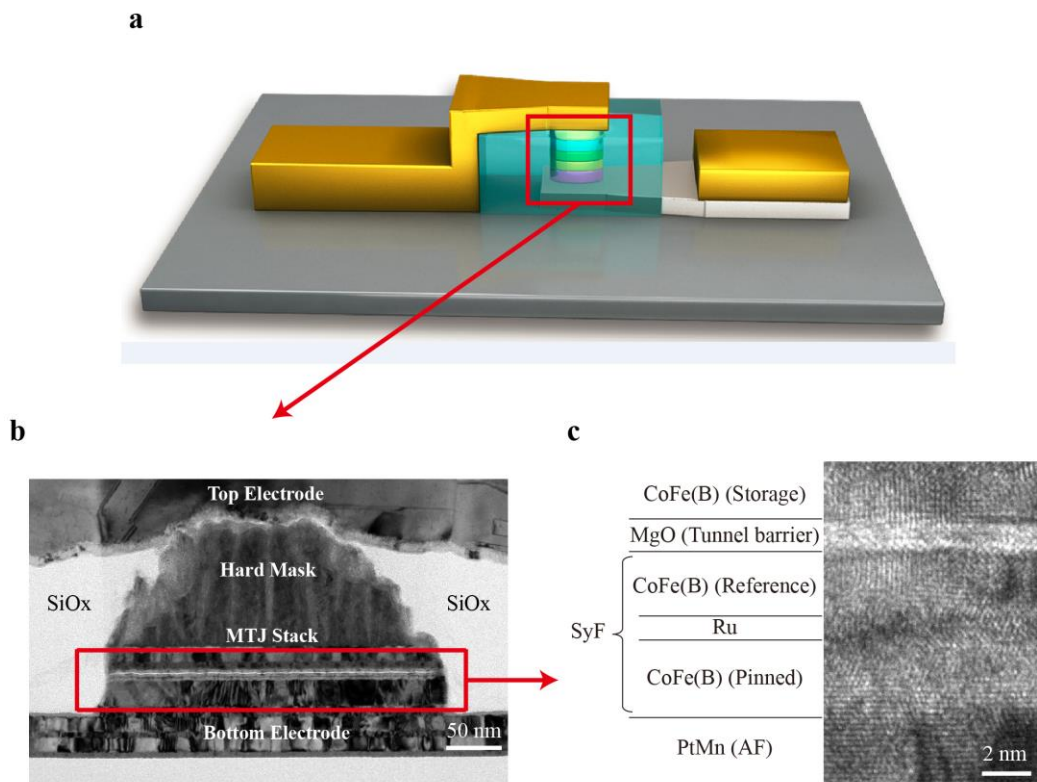


Figure 1

**Figure 1 | Re-MRAM device.** **a**, Schematic of the Re-MRAM device. A two-terminal MTJ nanopillar is encapsulated within a  $\text{SiO}_x$ -based matrix. **b**, TEM image of the Re-MRAM device. The top electrode, hard mask, MTJ stack (indicated with a red rectangular) and bottom electrode are indicated. **c**, HRTEM image of a CoFe(B)-MgO-based MTJ nanopillar. The free layer (CoFe(B)), tunnel barrier (MgO), synthetic ferri-magnetic (SyF) reference layer (CoFe(B)/Ru/CoFe(B)) and anti-ferromagnetic layer PtMn are indicated. A crystalline structure can be observed for both CoFe(B) and MgO.

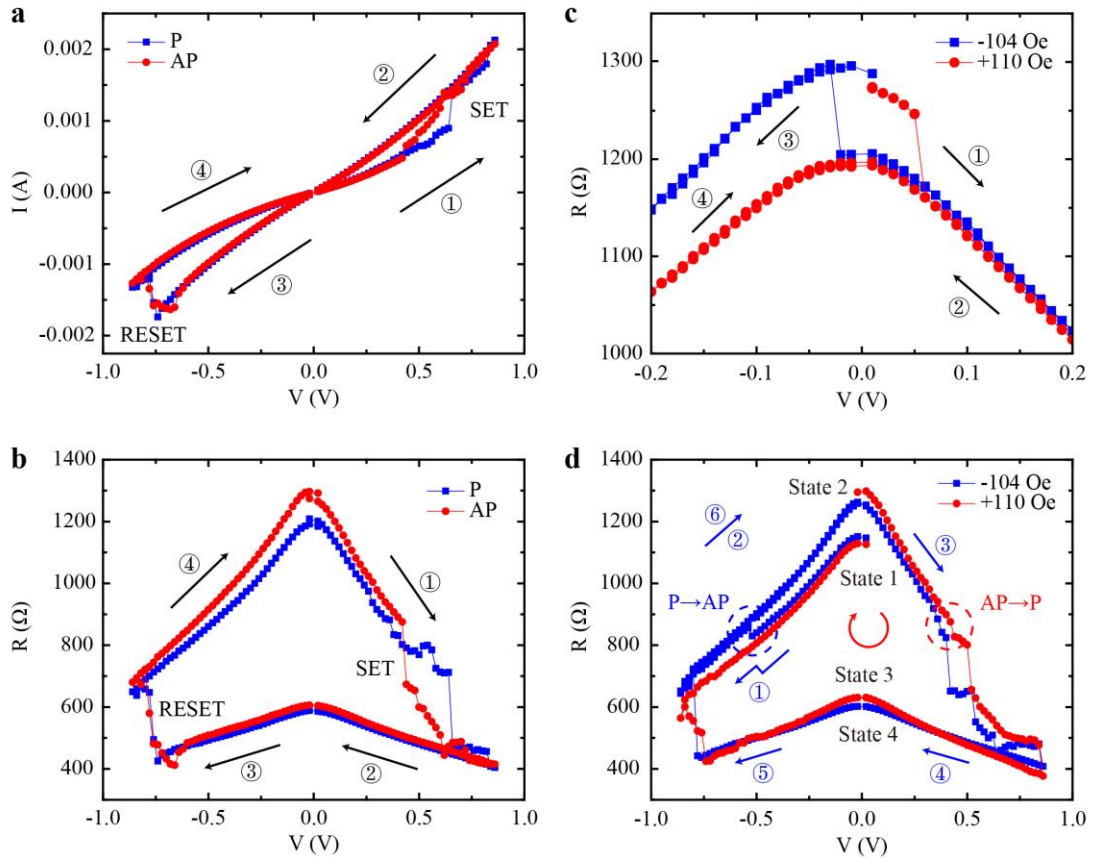


Figure 2

**Figure 2 | Transport properties of the Re-MRAM device.** The direction of the external magnetic field is along the easy axis of the ellipse. The arrows and numbers (1) ~ (6) indicate the voltage sweep direction. States 1 to 4 correspond to the resistive states described in Figure 5b. **a**, I-V curves without an applied magnetic field up to  $\pm 1$  V. The MTJ was set to either the P or AP configuration before the measurement. The SET and RESET voltages are indicated. **b**, Corresponding R-V curves of (a). **c**, R-V curves under external positive and negative magnetic fields for voltages below  $\pm 0.2$  V indicating pure CIMS without VIRS. **d**, R-V curves under external positive and negative magnetic fields up to  $\pm 1$  V. The VIRS process is observed near  $+0.5$  V (SET) and  $-0.7$  V (RESET). For the CIMS process, P to AP switching is observed near  $-0.5$  V for a magnetic field of  $-104$  Oe and near  $+0.4$  V for a magnetic field of  $+110$  Oe.

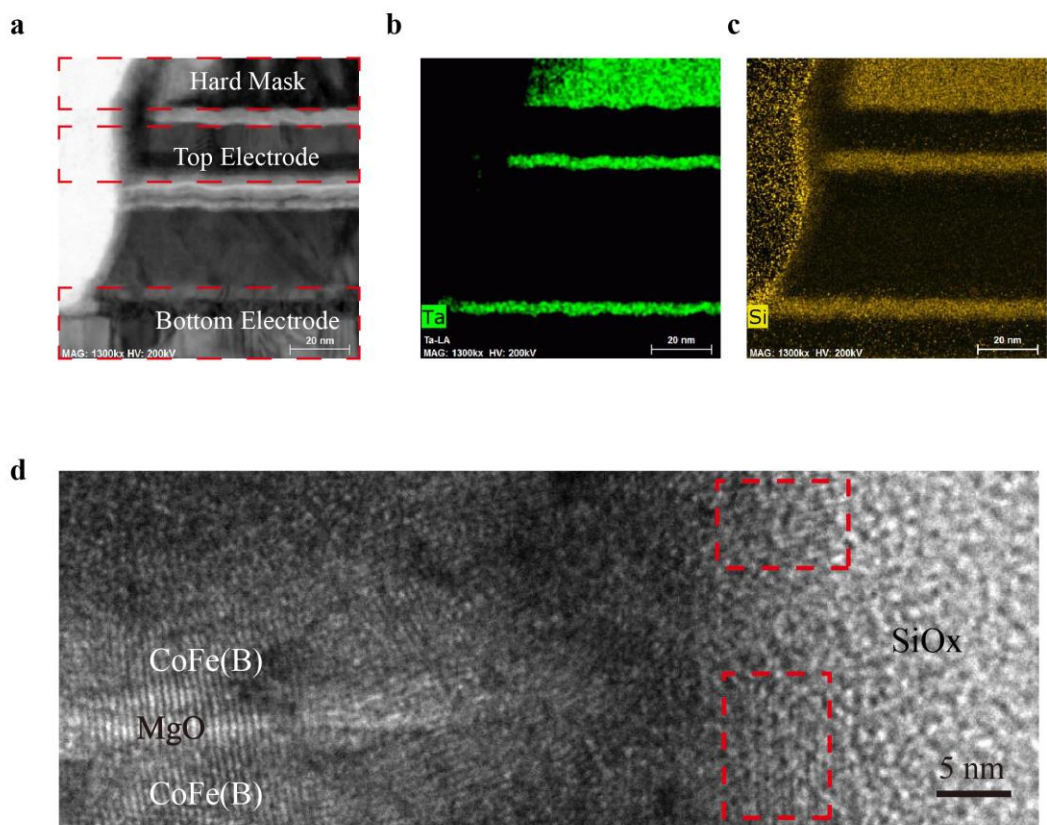


Figure 3

**Figure 3 | Microstructural characterization of the Re-MRAM device.** **a**, STEM image near the vertical edge of the MTJ nanopillar. The regions of the hard Ta mask, top electrode and bottom electrode are indicated by the red dashed rectangles. **b**, EDS mapping of Ta using the Ta- $L\alpha$  series line characteristic peaks. **c**, EDS mapping of Si using the Si- $K$  series line characteristic peaks. Note that since the Ta- $M\alpha$  (1.709 KeV) and Si- $K\alpha_1$  (1.739 KeV) peaks overlap; Ta is also detected. **d**, HRTEM image at the edges of the nanopillars. Nanocrystalline structures embedded in the SiO<sub>x</sub> matrix are indicated by the red dashed rectangles.

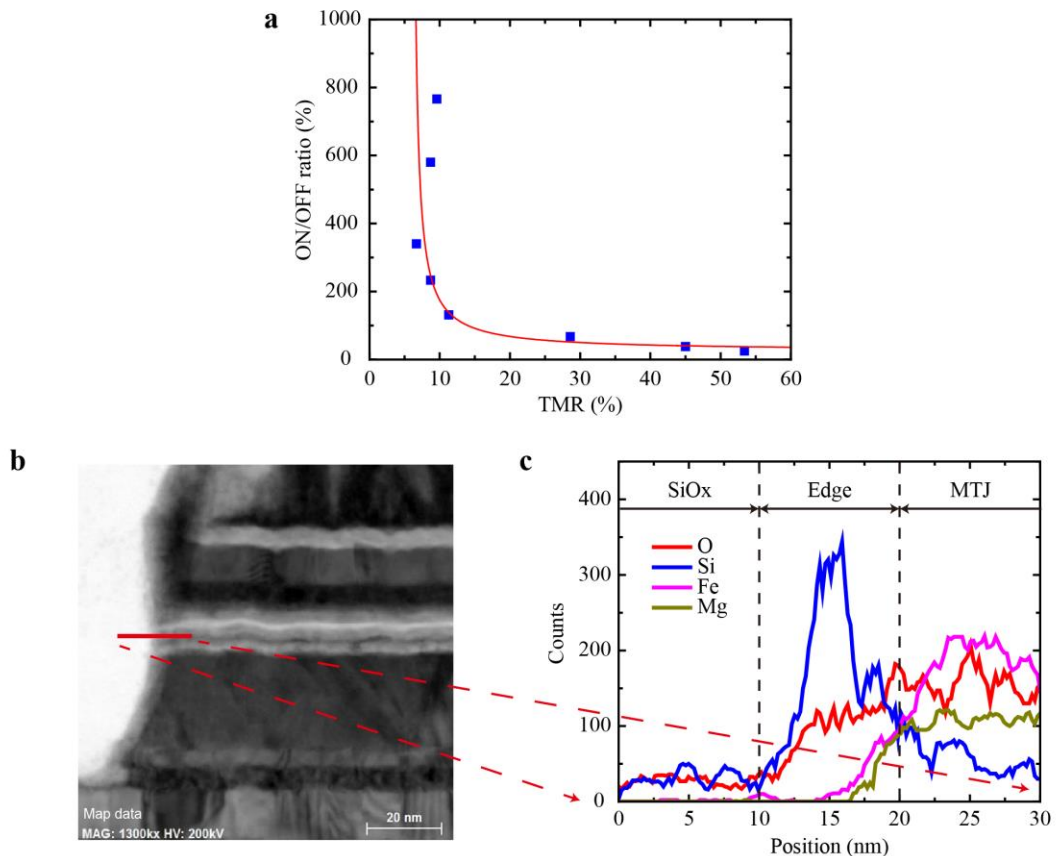


Figure 4

**Figure 4 | Transport and edge characterization of the Re-MRAM device.** **a**, Relationship between the ON/OFF ratio and the TMR ratio measured in different devices. The TMR was obtained through R-H measurements under a low voltage of 10 mV. The ON/OFF ratio was obtained after conducting a voltage (current) sweep. The blue squares are the experimental data, and the red line is a guide for the eyes. **b**, STEM image obtained using an HAADF detector. The EDS line-scan is marked in red and was measured from the  $\text{SiO}_x$  matrix into the MTJ nanopillar. **c**, EDS line-scan for O, Si, Fe and Mg corresponding to the red line indicated in (b). Three different regions can be delimited: a pure  $\text{SiO}_x$  region, an intermixed layer with an aggregation of Si and O (10 nm) and an MTJ region.

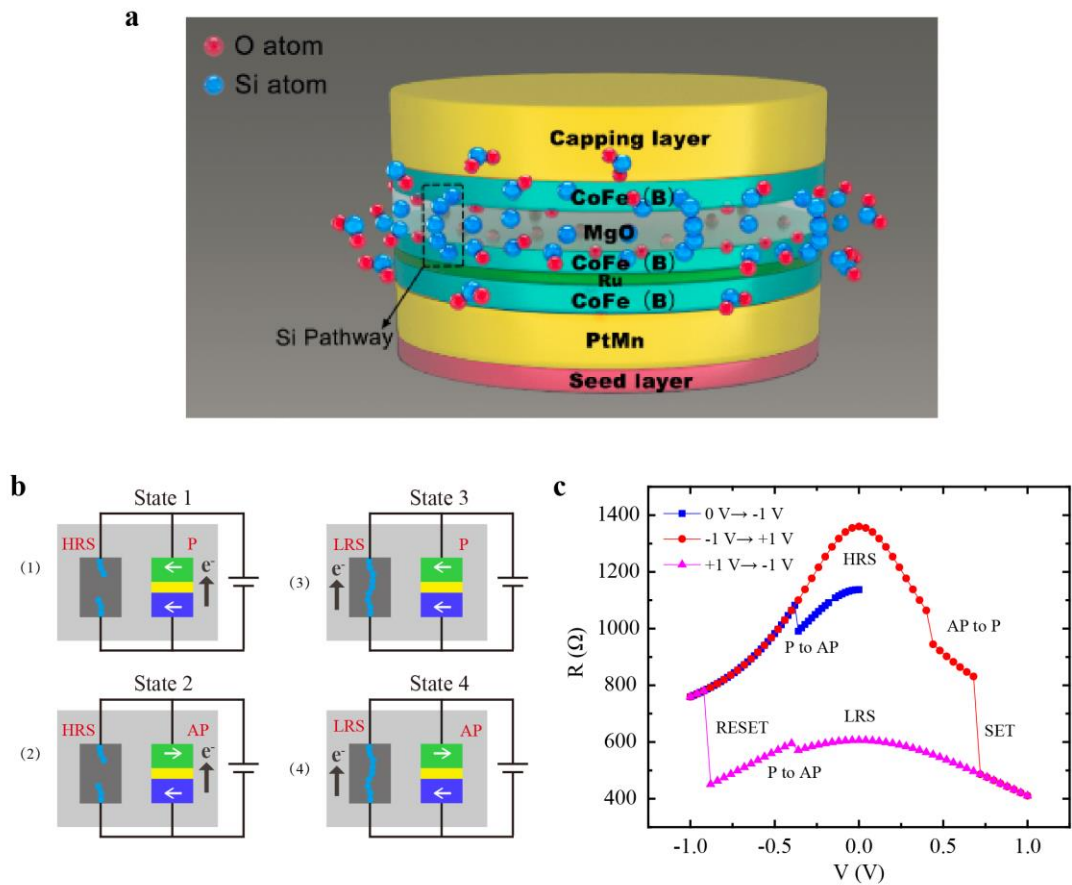


Figure 5

**Figure 5 | Resistance switching model of the Re-MRAM device.** **a**, Schematic of the MTJ nanopillar surrounded by Si filaments. The blue and red balls represent the Si atoms and oxygen atoms, respectively. **b**, Resistive model corresponding to a RRAM element in parallel with a MRAM element. Depending on the configuration of the RRAM and MRAM elements, four different states can be obtained in the Re-MRAM device. The blue balls represent the conductive filaments made of the Si pathway. States 1 - 4 correspond to those in Fig. 2d. **c**, Simulation of the R-V behaviour using a physical-based model of STT-MTJ and an MIM resistive junction connected in parallel. A magnetic field was not included in the simulation.

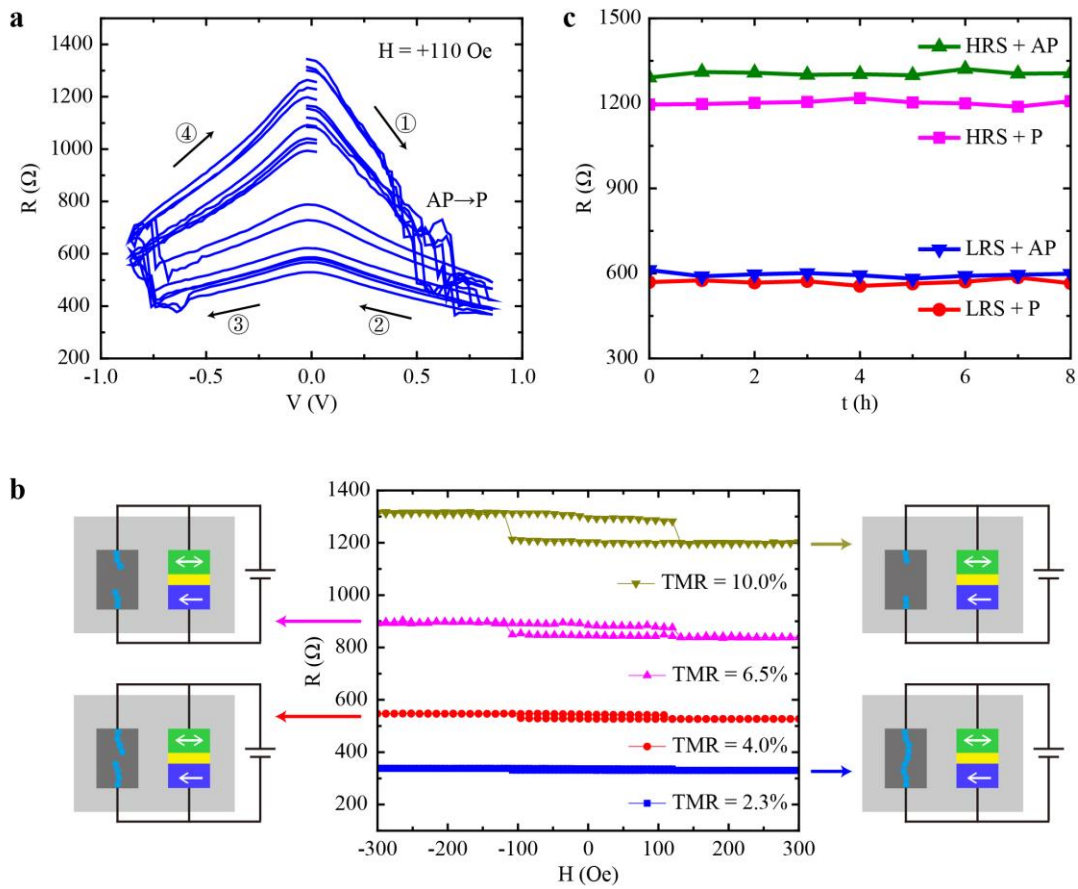


Figure 6

**Figure 6 | Multilevel resistance states in the Re-MRAM device.** **a**, Seven different R-V curves under external magnetic fields in the same device. **b**, R-H hysteresis loops with different initial resistive states for the same device. The measurements were conducted from an LRS (approximately  $600 \Omega$ ) to an HRS (approximately  $1300 \Omega$ ). **c**, Time-independent resistance curves showing the non-volatile features of the Re-MRAM for four different resistive states (LRS+AP, LRS+P, HRS+AP and HRS+P).